1-1-2006

Probing Nanoscale Ferroelectricity by Ultraviolet Raman Spectroscopy

Dmitri Tenne
Boise State University

A. Bruchhausen
Centro Atomico Bariloche & Instituto Balseiro

N. D. Lanzillotti-Kimura
Centro Atomico Bariloche & Instituto Balseiro

A. Fainstein
Centro Atomico Bariloche & Instituto Balseiro

R. S. Katiyar
University of Puerto Rico

See next page for additional authors

Science, 313, 1614 (2006)

Probing Nanoscale Ferroelectricity by Ultraviolet Raman Spectroscopy

D. A. Tenne,[1*] A. Bruchhausen,[2] N. D. Lanzillotti-Kimura,[2] A. Fainstein,[2] R. S. Katiyar,[3] A. Cantarero,[4] A. Soukiassian,[5] V. Vaithyanathan,[5] J. H. Haeni,[5] W. Tian,[5] D. G. Schlom,[5] K. J. Choi,[6] D. M. Kim,[6] C. B. Eom,[6] H. P. Sun,[7] X. Q. Pan,[7] Y. L. Li,[5,8] L. Q. Chen,[5] Q. X. Jia,[8] S. M. Nakhmanson,[9] K. M. Rabe,[9] X. X. Xi[1,5]

[1]Department of Physics, The Pennsylvania State University, University Park, PA 16802, USA

[2]Centro Atómico Bariloche & Instituto Balseiro, C.N.E.A., 8400 San Carlos de Bariloche, Argentina

[3]Department of Physics, University of Puerto Rico, San Juan, Puerto Rico 00931-3343, USA

[4]Materials Science Institute, University of Valencia, P.O. Box 22085, E-46071 Valencia, Spain

[5]Department of Materials Science and Engineering, The Pennsylvania State University, University Park, PA 16802, USA

[6]Department of Materials Science and Engineering, University of Wisconsin, Madison, WI 53706, USA

[7]Department of Materials Science and Engineering, The University of Michigan, Ann Arbor, MI 48109, USA

[8]Materials Science and Technology Division, Los Alamos National Laboratory, Los Alamos, New Mexico 87545, USA

[9]Department of Physics and Astronomy, Rutgers, the State University of New Jersey, 136 Frelinghuysen Road, Piscataway, NJ 088548019, USA

[*]To whom correspondence should be addressed; E-mail: dat10@psu.edu.

We demonstrate that ultraviolet Raman spectroscopy is an effective technique to measure the transition temperature, T_c, accurately in ferroelectric ultrathin films and superlattices. We show that one-unit-cell thick $BaTiO_3$ layers in $BaTiO_3$/$SrTiO_3$ superlattices are not only ferroelectric (T_c as high as 250 K), but also polarize the quantum paraelectric $SrTiO_3$ layers adjacent to them. T_c was tuned by $\sim$ 500 K by varying the thicknesses of $BaTiO_3$ and $SrTiO_3$ layers, revealing the essential roles of electrical and mechanical boundary conditions for nanoscale ferroelectricity.

Ferroelectricity at the nanoscale has emerged as fertile ground for new physical phenomena and devices (*1–3*). Shrinking dimensions demand characterization techniques capable of probing the properties of ferroelectrics in, for example, ultrathin films and superlattices. In particular, it is difficult to measure the ferroelectric phase transition temperature T_c in such systems, and the T_c information is largely missing or inaccurate in reports of ferroelectricity in nanoscale ultrathin films and superlattices (*3–5*). One fundamental property of ferroelectrics that changes qualitatively during the phase transition is the dynamics of lattice vibrations (*6*). Thus, its temperature dependence allows determination of T_c. While lattice dynamics in ferroelectric films (*7,8*) and superlattices (*9*) from 150 nm to 2 μm in thickness have been investigated previously, such studies are very difficult for films thinner than $\sim$ 100 nm. We report the use of ultraviolet (UV) Raman spectroscopy on $BaTiO_3$/$SrTiO_3$ superlattices with total thicknesses down to 24 nm, which enabled us to measure T_c of the $BaTiO_3$ layers in the superlattices. We found that the $BaTiO_3$ layers are ferroelectric even when their thickness is only one unit cell (0.4 nm), and that they can induce polarization in the adjacent paraelectric $SrTiO_3$ layers that are much thicker. By varying the thickness of both the $BaTiO_3$ and $SrTiO_3$ layers, T_c was tuned from 250 K below to 235 K above the bulk value of $BaTiO_3$ (403 K). The result shows that under favorable electrical and mechanical boundary conditions ferroelectricity is robust in nanoscale

systems.

Conventional visible Raman spectroscopy works poorly for thin films of ferroelectrics and other wide-bandgap materials because the visible photon energy is much smaller than the bandgap (*10*). Consequently, the absorption is extremely weak and the penetration depth is large, allowing light to travel through the film into the substrate, which generates overwhelming signals in the Raman spectra. For UV excitation, the photon energy is above the bandgaps of ferroelectrics, leading to a much stronger absorption and a shorter penetration depth, preventing light from entering the substrate. UV excitation near the bandgap also leads to strong resonance enhancement of Raman signals. This is demonstrated by Fig. 1 where Raman spectra of a $BaTiO_3$/$SrTiO_3$ superlattice measured with visible (514.5 nm) and UV (351.1 nm) excitations are shown. The substrate features dominate the 514.5 nm spectrum while they are greatly reduced in the UV spectrum, in which peaks of superlattice phonons are clearly observed.

UV Raman spectroscopy has not been widely used for ferroelectric films because of technical difficulties such as lower throughput efficiency, insufficient dispersion, and higher stray light level of UV Raman spectrometers compared to those operating in the visible range. Recently, room temperature measurement of $SrTiO_3$ films using 325 nm excitation has been reported (*11*). The recent progress in UV Raman instrumentation has made measurement of ferroelectric films possible. In our experiment, a triple monochromator was used to provide high resolution and effective stray light reduction (*12*). Powerful laser sources and optimized optical paths were used to improve the throughput. With these setups, we have measured Raman scattering in $BaTiO_3$/$SrTiO_3$ superlattices as thin as 24 nm, and in $(Ba_{0.5}Sr_{0.5})TiO_3$ films 10 nm in thickness.

The $BaTiO_3$/$SrTiO_3$ superlattices are denoted by $(BTO_n/STO_m)\times$ number of periods, where n and m refer to the thickness, in unit cells, of the $BaTiO_3$ and $SrTiO_3$ layers, respectively. They were all grown on (001) $SrTiO_3$ substrates. Details of the sample preparation by reactive molecular-beam epitaxy (*13*) and structural characterization are presented in Supporting Online

Material (*12*).

Curve 3 in Fig. 1 is typical of the UV Raman spectra of $BaTiO_3$/$SrTiO_3$ superlattices below T_c, exhibiting strong first-order (single-phonon) peaks as labeled in the figure. Weak second-order (two-phonon) features from the $SrTiO_3$ substrate can be seen between 600 and 700 cm^{-1} and as a background in the range 200-500 cm^{-1}. The phonon mode assignment is made by comparison with the spectra of $SrTiO_3$ and $BaTiO_3$ single crystals (*12*) and with the help of first-principles calculations. The lines at about 290 cm^{-1} have similar positions and shapes to the TO_2 modes of A_1 symmetry of the tetragonal-phase $BaTiO_3$ (*14, 15*), thus they are assigned to the $BaTiO_3$ layers. The line at about 180 cm^{-1} corresponds closely to the TO_2 line in the electric-field-induced Raman spectrum of $SrTiO_3$ crystals (*16*). It is not from the $SrTiO_3$ substrate because the first-order Raman lines are symmetry-forbidden in bulk $SrTiO_3$ (*17*). Although the TO_1 mode of A_1 symmetry of $BaTiO_3$ is at about the same position (177 cm^{-1}), it has markedly different relative intensity and shape (*14*) from the 180-cm^{-1} line. Therefore, we attribute this line to the TO_2 phonon in the $SrTiO_3$ layers. The LO_3 and TO_4 modes involve both $SrTiO_3$ and $BaTiO_3$ layers and extend through the superlattice. A doublet of folded longitudinal acoustic (LA) phonon due to the superlattice periodicity (*18*) is also observed. The two triangles indicate the predicted first doublet frequencies by an elastic continuum model (*19*). The observation of the LA phonon folding suggests that these superlattices possess the requisite structural quality for acoustic Bragg mirrors and cavities used for coherent phonon generation (*20, 21*).

Bulk crystalline $BaTiO_3$ is cubic and paraelectric above T_c = 403 K, becomes tetragonal and ferroelectric below T_c, and goes through additional transitions to orthorhombic at 278 K and rhombohedral at 183 K (*22*). Bulk crystalline $SrTiO_3$ is paraelectric at all temperatures due to quantum fluctuations (*23*). The temperature evolution of Raman spectra for two superlattice samples is shown in Fig. 2: **A** $(BTO_2/STO_{13})\times 20$ and **B** $(BTO_8/STO_4)\times 10$. The shapes and positions of the $BaTiO_3$ lines at low temperatures are characteristic of $BaTiO_3$ in the tetragonal

phase (*12, 14, 15*), indicating that the $BaTiO_3$ layers are tetragonal and ferroelectric below T_c. The presence of the first-order Raman lines of $SrTiO_3$ shows that the $SrTiO_3$ layers are polar because the first-order lines are symmetry-forbidden in non-polar $SrTiO_3$ (*17*). The intensities of the first-order superlattice phonons decrease as the temperature increases and disappear at T_c. Above T_c, the spectra contain only the second-order features as expected from the symmetry selection rules. When the $BaTiO_3$ layers are paraelectric, the induced polarization in the $SrTiO_3$ layers also disappears.

By plotting the first-order Raman intensity as a function of temperature, we can determine T_c accurately as the temperature where the intensity becomes zero. For this purpose, the TO_2 and TO_4 phonon lines are the most suitable because they do not overlap with the second-order features. The results, with the phonon intensities normalized by the Bose factor $n + 1 = (1 - \exp(-\hbar\omega/kT))^{-1}$ and by the intensities at 7 K, are presented for four superlattices: $(BTO_2/STO_4)\times 40$ and $(BTO_5/STO_4)\times 25$ in Fig. 3**A**, and $(BTO_8/STO_4)\times 10$ and $(BTO_8/STO_4)\times 40$ (strain partially relaxed) in Fig. 3**B**. Both TO_2 and TO_4 phonons show similar behaviors and the dashed-dotted lines are linear fits to the average of the two modes. The linear fit corresponds to a parabolic decrease of polarization with temperature as Raman intensity is proportional to the square of atomic displacement. The intersection of a dash-dotted line with the horizontal axis is taken as the T_c of the sample.

The temperature dependence of polarization from a phase-field model calculation (*24*) is plotted in Figs. 3**C** and 3**D** for the same samples as in Figs. 3**A** and 3**B**. The model assumes that the $BaTiO_3$ and $SrTiO_3$ layers in the superlattices have their respective bulk elastic and thermodynamic properties. The in-plane lattice constant is commensurately constrained to the $SrTiO_3$ substrate except for the partially relaxed case, and the top surface is stress-free. The surface depolarization field is ignored and a short-circuit electrostatic boundary condition is employed. A computational cell of 64 nm along the two in-plane directions and one unit cell along the

growth direction was employed. The corresponding 3-dimensional time-dependent Ginzburg-Landau equations are then numerically solved using the perturbation method with semi-implicit Fourier-spectral algorithms (*25*). The result reveals a spontaneous polarization along the growth direction with multiple 180° domains in the $BaTiO_3$ layers, which induces polarization in the adjacent $SrTiO_3$ layers whose magnitude and distribution vary with the thickness and domain size of the $BaTiO_3$ layers. The spontaneous polarization in the $BaTiO_3$ layers becomes zero at T_c, and the predicted T_c values agree with those from the Raman data. This is remarkable considering that no fitting parameters from the Raman experiments are used in the calculations.

In Fig. 4, T_c determined by the Raman data, XRD, and the phase-field model are shown as a function of the $BaTiO_3$ and $SrTiO_3$ layer thicknesses. The XRD measurement provides an additional confirmation of the Raman results, where a change in the temperature dependence of the out-of-plane lattice constant can be taken as an indication of T_c (*12*). The figure shows that the $BaTiO_3$ layers in the superlattices are ferroelectric even when their thickness is only one unit cell, with a T_c as high as 250 K. T_c increases with increasing n as the dipole-dipole interaction in $BaTiO_3$ layers becomes stronger, while large m suppresses T_c by reducing the coupling between the $BaTiO_3$ layers. By changing the values of n and m, we were able to tune T_c from 151 K to 638 K, i.e. from 250 K below to 235 K above the bulk value of $BaTiO_3$. The higher-than-bulk T_c is due to the strain in the $BaTiO_3$ layers, just as strain enhances T_c in single-layer ferroelectric films (*26, 27*). When the strain is partially relaxed in sample $(BTO_8/STO_4)\times 40$, T_c drops almost to the bulk $BaTiO_3$ value. While the 3-dimensional phase-field model allowing domain formation provides a good description of the Raman data, simulations assuming a single domain in the $BaTiO_3$ layers yield significantly lower T_c for $m = 13$, demonstrating the importance of domain formation in theoretical calculations (*28*).

We now can conclude that ferroelectricity can be very strong in one-unit-cell thick $BaTiO_3$ layers ($T_c \sim$ 250 K for n/m = 1/4). The electrical boundary condition plays a critical role.

With the highly-polarizable $SrTiO_3$ in contact with the $BaTiO_3$ layers, the critical thickness is reduced to a single unit cell. Meanwhile, the mechanical boundary condition imposed by the $SrTiO_3$ substrate leads to strain in the $BaTiO_3$ layers and thus enhanced ferroelectricity. The interplay between the electrical and mechanical boundary conditions enables the tuning of T_c by nearly 500 K.

References and Notes

1. C. H. Ahn, K. M. Rabe, J.-M. Triscone, *Science* **303**, 488 (2004).

2. J. Junquera, P. Ghosez, *Nature (London)* **422**, 506 (2003).

3. D. D. Fong, *et al.*, *Science* **304**, 1650 (2004).

4. T. Tybell, C. H. Ahn, J. -M. Triscone, *Appl. Phys. Lett.* **75**, 856 (1998).

5. H. N. Lee, H. M. Christen, M. F. Chisholm, C. M. Rouleau, D. H. Lowndes, *Nature* **433**, 395 (2005).

6. M. E. Lines, A. M. Glass, *Principles and applications of ferroelectrics and related materials* (Clarendon Press, Oxford, 1977).

7. A. A. Sirenko, *et al.*, *Nature (London)* **404**, 373 (2000).

8. T. Ostapchuk, *et al.*, *Phys. Rev. B* **66**, 235406 (2002).

9. R. S. Katiyar, Y. I. Yuzyuk, R. R. Das, P. Bhattacharya, V. Gupta, *Ferroelectrics* **329**, 907 (2005).

10. K. van Benthem, C. Elsässer, R. H. French, *J. Appl. Phys.* **90**, 6156 (2001).

11. L. H. Tisinger, *et al.*, *J. Vac. Sci. Technol. B* **21**, 53 (2003).

12. See Supporting Online Material for details .

13. D. G. Schlom, *et al.*, *Mater. Sci. Eng. B* **87**, 282 (2001).

14. A. Scalabrin, A. S. Chaves, D. S. Shim, S. P. S. Porto, *Phys. Status Solidi B* **79**, 731 (1977).

15. D. A. Tenne, *et al.*, *Phys. Rev. B* **69**, 174101 (2004).

16. P. A. Fleury and J. M. Worlock, *Phys. Rev.* **174**, 613 (1968).

17. W. G. Nilsen and J. G. Skinner, *J. Chem. Phys.* **48**, 2240 (1968).

18. B. Jusserand, M. Cardona, *Light Scattering in Solids V* (Springer, Heidelberg, 1989), pp. 49-152.

19. C. Colvard, *et al.*, *Phys. Rev. B* **31**, 2080 (1985).

20. M. Trigo, A. Bruchhausen, A. Fainstein, B. Jusserand, V. Thierry-Mieg, *Phys. Rev. Lett.* **89**, 227402 (2002).

21. A. Bartels, T. Dekorsy, H. Kurz, K. Köhler, *Phys. Rev. Lett.* **82**, 1044 (1999).

22. L. E. Cross, *Ferroelectric ceramics*, N. Setter, E. L. Colla, eds. (Birkhäuser Verlag, Basel, 1993), p. 1.

23. K. A. Müller, H. Burkard, *Phys. Rev. B* **19**, 3593 (1979).

24. L.-Q. Chen, *Annu. Rev. Mater. Res.* **32**, 113 (2002).

25. L.-Q. Chen, J. Shen, *Comput. Phys. Commun.* **108**, 147 (1998).

26. K. J. Choi, *et al.*, *Science* **306**, 1005 (2004).

27. J. H. Haeni, *et al.*, *Nature (London)* **430**, 758 (2004).

28. V. A. Stephanovich, I. A. Luk'yanchuk, M. G. Karkut, *Phys. Rev. Lett.* **94**, 047601 (2005).

29. We thank Leah Bergman for her help in the early stage of this work. This work was partially supported by DOE under Grant No. DE-FG02-01ER45907 (Xi), by ONR under Grant Nos. N00014-03-1-0721 (Schlom), N00014-04-1-0426 (Schlom), N00014-03-1-0534

P0005 (Fainstein), N00014-05-1-0559 (Eom), N00014-00-1-0261 (Rabe), and N00014-01-1-0365 (Rabe), by NASA under Grant No. NASA3-NCC1034 (Katiyar), by NSF under Grant Nos. DMR-0507146 (Schlom, Chen, Pan, Rabe, Xi), DMR-0122638 (Chen), DMR-0313764 (Eom), ECS-0210449 (Eom), and DMR-0315633 (Pan), and by a Guggenheim fellowship (Chen). The work at Los Alamos National Laboratory was supported by the Laboratory-Directed Research and Development Program under US DOE.

Fig. 1. Room temperature Raman spectra of (1) a bare $SrTiO_3$ substrate (black curve), (2) a $(BTO_5/STO_4)\times 25$ superlattice (T_c = 530 K, blue curve) measured with visible excitation (514.5 nm), and (3) the same superlattice measured with 351.1 nm UV excitation (red curve). The dashed black line shows the bare $SrTiO_3$ substrate spectrum measured with 351.1 nm UV excitation. Triangles show the calculated frequencies of the first folded LA doublet.

Fig. 2. Temperature evolution of UV Raman spectra of superlattices **A** $(BTO_2/STO_{13})\times 20$ and **B** $(BTO_8/STO_4)\times 10$. The arrows mark the $SrTiO_3$-like TO_2 mode at 180 cm^{-1} and the TO_4 mode at about 530 cm^{-1}, whose intensities decrease as the temperature increases and disappear at T_c.

Fig. 3. Temperature dependencies of normalized Raman intensities of TO_2 (solid triangles) and TO_4 (open triangles) phonons for **A** $(BTO_2/STO_4)\times 40$ and $(BTO_5/STO_4)\times 25$ and **B** $(BTO_8/STO_4)\times 10$ and $(BTO_8/STO_4)\times 40$. Sample $(BTO_8/STO_4)\times 40$ is partially relaxed while the other three samples are commensurate with the $SrTiO_3$ substrate. The dash-dotted lines are fits to a linear temperature dependence. **C** and **D**: The 3-dimensional phase-field model calculations of polarization as a function of temperature in the same superlattice samples. Polarization is given as a fraction of the polarization of bulk $BaTiO_3$, P_0 = 0.26 C/m^2.

Fig. 4. Dependence of T_c on n and m in superlattices BTO_n/STO_m. Blue symbols are for m = 4 and red symbols for m = 13. Open triangles are from temperature-dependent XRD measurement. Circles with lines are from the 3-dimensional phase-field model calculations. The black dash-dotted line shows the T_c in bulk $BaTiO_3$.

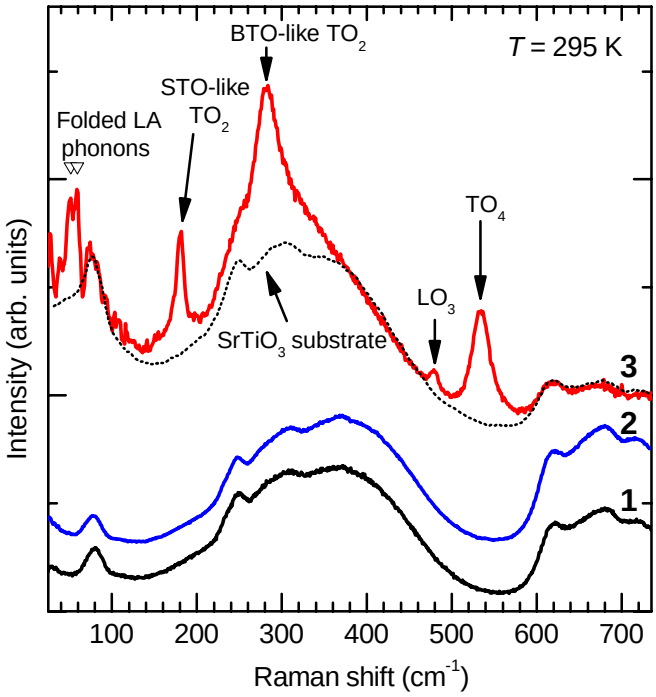

Figure 1

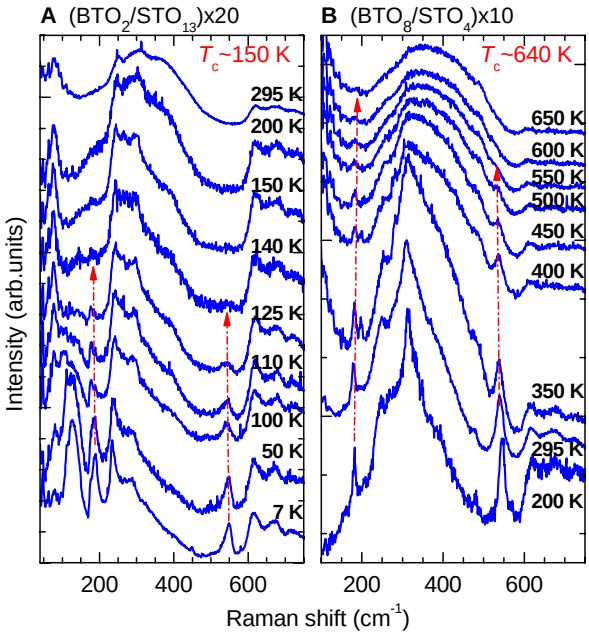

Figure 2

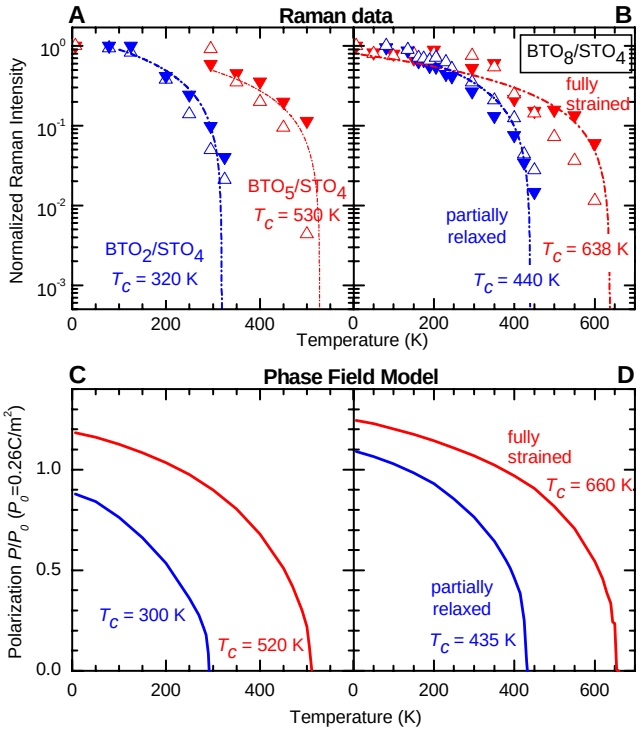

Figure 3

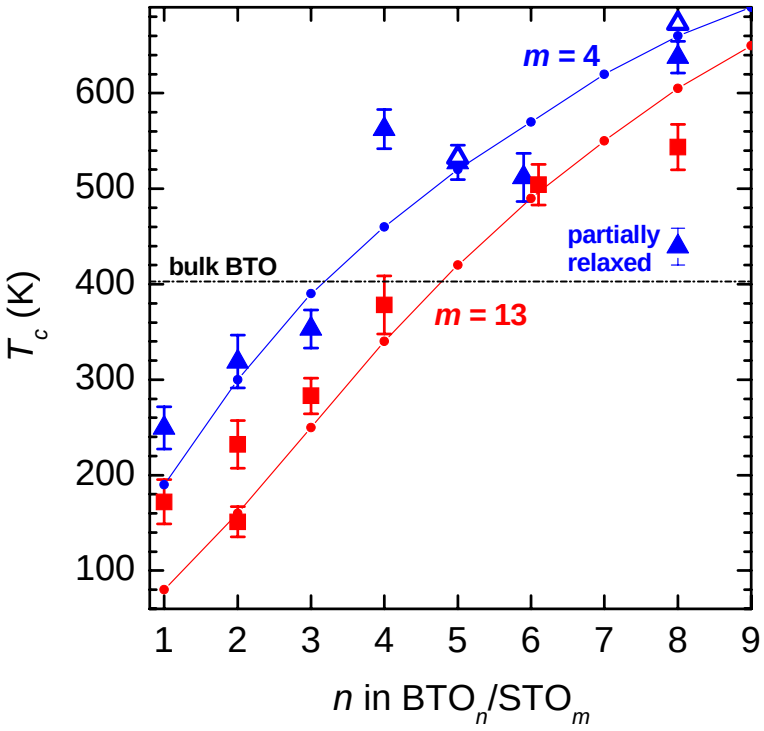

Figure 4

Supporting Online Material

Materials and Methods

1. Preparation and structural characterization of $BaTiO_3/SrTiO_3$ superlattices

The $BaTiO_3/SrTiO_3$ superlattice samples were grown by reactive molecular-beam epitaxy *(1)*. The substrate is (001) $SrTiO_3$ terminated at the TiO_2 layer, with BaO being the first layer deposited. The n and m values are controlled using reflection high-energy electron diffraction (RHEED) oscillations during growth, and confirmed by x-ray diffraction (XRD) and in some samples by high resolution transmission electron microscopy (HRTEM) *(2)*. XRD shows excellent epitaxy and crystallinity in the superlattice samples, with all superlattice peaks present in the $\theta - 2\theta$ scan. HRTEM images show atomically sharp $BaTiO_3/SrTiO_3$ interfaces and acurate periodicity *(2)*. According to XRD, all samples are commensurate to the $SrTiO_3$ substrate ($a = 0.3905$ nm), meaning that the $SrTiO_3$ layers are strain free and the $BaTiO_3$ layers are under 2.2% compressive biaxial strain ($a = 0.3992$ nm in bulk $BaTiO_3$ at room temperature), except for a 200 nm thick superlattice $(BTO_8/STO_4)\times 40$ in which the strain is partially relaxed ($a = 0.3946$ nm in-plane). In this case, the $SrTiO_3$ layers are under biaxial tensile strain and the $BaTiO_3$ layers are under biaxial compressive strain. Some samples were annealed in oxygen (760 Torr, 550°C, 5 hours) to reduce the population of oxygen vacancies, and we found no observable effect of the annealing on the Raman spectra.

As an example of the structural characterization of the superlattice samples in this work, the four-circle x-ray diffraction (XRD) scans (Figs. S1–S3) and a high resolution transmission electron microscopy (HRTEM) image for the superlattice $(BTO_5/STO_4)\times 25$ (Fig. S4) are presented here.

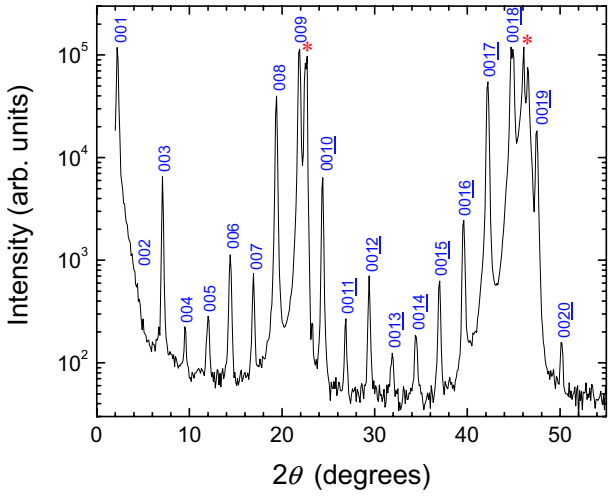

Figure S1. An x-ray diffraction $\theta - 2\theta$ scan of the $(BTO_5/STO_4)\times 25$ superlattice using Cu K_α radiation. Substrate peaks are marked by asterisks ($*$). All superlattice peaks are present for $2\theta < 55°$, indicating atomically sharp interfaces between $BaTiO_3$ and $SrTiO_3$ layers and acurate periodicity. An out-of-plain lattice parameter, $c = 36.3 \pm 0.1$ Å, was obtained from a Nelson-Riley analysis *(3)*, which is consistent with 5 unit cells of $BaTiO_3$ and 4 unit cells of $SrTiO_3$ in a period.

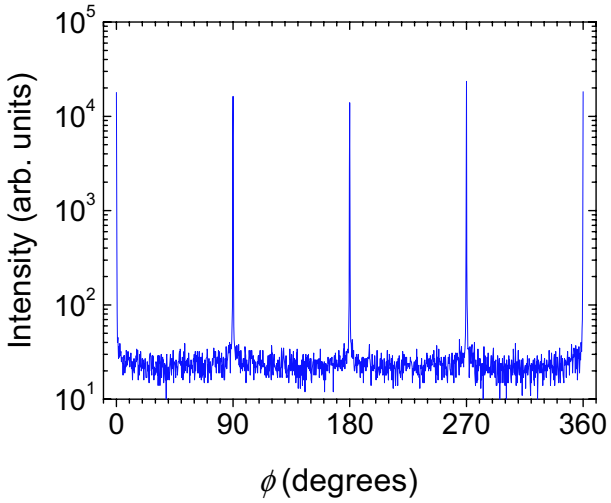

Figure S2. An x-ray diffraction ϕ scan of the 108 peak taken at $\chi = 40.7°$ of the $(BTO_5/STO_4)\times25$ superlattice. In this scan $\phi = 0°$ is aligned parallel to the [100] in-plain direction of the substrate and $\chi = 90°$ aligns the diffraction vector to be perpendicular to the plane of the substrate. It shows that the superlattice is epitaxial with the expected ([100] superlattice ∥ [100] substrate) in-plane alignment with the substrate.

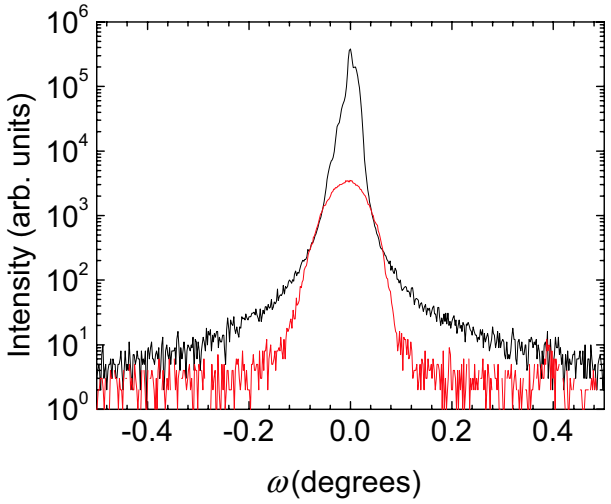

Figure S3. Rocking curves of the $(BTO_5/STO_4)\times25$ superlattice 00$\underline{18}$ peak (red) of the $(BTO_5/STO_4)\times25$ superlattice and the underlying $SrTiO_3$ substrate 002 peak (black). The full width at half maximum (FWHM) is 0.034° for the superlattice peak as compared to 0.013° for the substrate peak. The sharp rocking curve indicates the high structural perfection of the superlattice.

2. UV Raman Measurement

In the present work, we used UV-optimized Jobin Yvon T64000 triple spectrometers with a multichannel coupled charge-device detector. The system employs a triple monochromator to provide high resolution and effective stray light reduction. Powerful laser sources and optimized optical paths were used to improve the throughput. Spectra were recorded in a backscattering geometry from 7 - 700 K using either a closed cycle cryostat (for low temperatures) or an evacuated heater

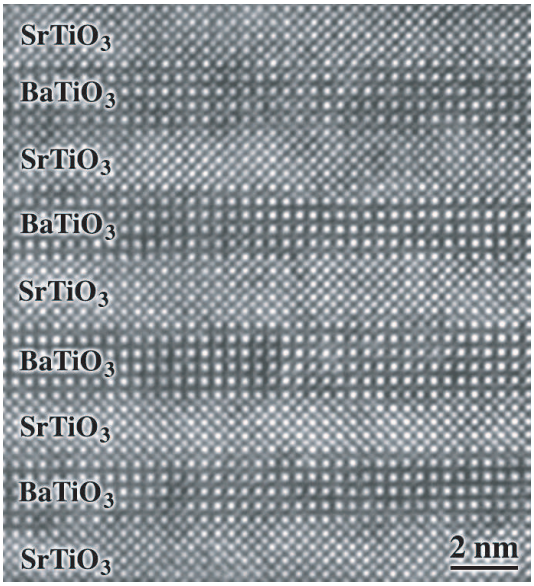

Figure S4. A cross-sectional HRTEM image of the superlattice. It shows alternating layers of 5 unit cells of $BaTiO_3$ and 4 unit cells of $SrTiO_3$, confirming the intended superlattice periodicity and the XRD result. The interfaces are abrupt and the roughness is within 1 unit cell.

stage (for above 300 K). The 351.1 nm line of an Ar^+ laser and the 325 nm line of a He-Cd laser were used for excitation.

We used low laser power densities (about 3.5 W/cm^2) to avoid possible heating of the scattering volume. To estimate the possible laser heating effect we measured the spectra of silicon at the same conditions. The Si phonon frequency has a linear dependence on temperature in the range 200 - 800 K *(4,5)*, decreasing by 0.5 cm^{-1} for every 20 degrees. Such a shift can be easily detected by Raman spectroscopy, which is a very sensitive technique to detect relative shifts of phonon lines (especially when measuring with a multichannel detector and keeping the same position of the monochromator). We did not observe any shifts of the Si phonon line while varying the laser power densities in the range 1 - 10 W/cm^2. Therefore, we can conclude that the laser heating effect for the Si sample is less than 10 degrees in the conditions we used. Although Si has higher thermal conductivity compared to $BaTiO_3$ and $SrTiO_3$, it also has about 10 times stronger absorption in the UV range used in our experiments. Hence, one can expect that the laser heating effect in the $BaTiO_3/SrTiO_3$ superlattices is not larger than in Si. The spectra of the $(BTO_5/STO_4)\times25$ superlattice ($T_c \approx 530$ K) measured at room temperature with laser power density varied from 1 to 10 W/cm^2 did not reveal any noticeable changes in the relative intensities of phonon lines in the spectra.

3. Phonon Mode Assignment

Figure S5 shows the comparison of room temperature spectra of two superlattices, $(BTO_8/STO_4)\times10$ and $(BTO_5/STO_4)\times25$, ($T_c = 640$ and 530 K, respectively) with the spectra of $BaTiO_3$ single crystals in the three different ferroelectric phases (tetragonal, orthorhombic, and rhombohedral) *(6)* and the $SrTiO_3$ substrate spectra at 295 and 5 K.

The lines at about 290 cm^{-1} have similar positions and shapes to the TO_2 modes of A_1 symmetry of $BaTiO_3$ in the tetragonal phase, thus we assign them to the $BaTiO_3$ layers and conclude that they are tetragonal. This is supported by the absence of the sharp peak at 310 cm^{-1} characteristic

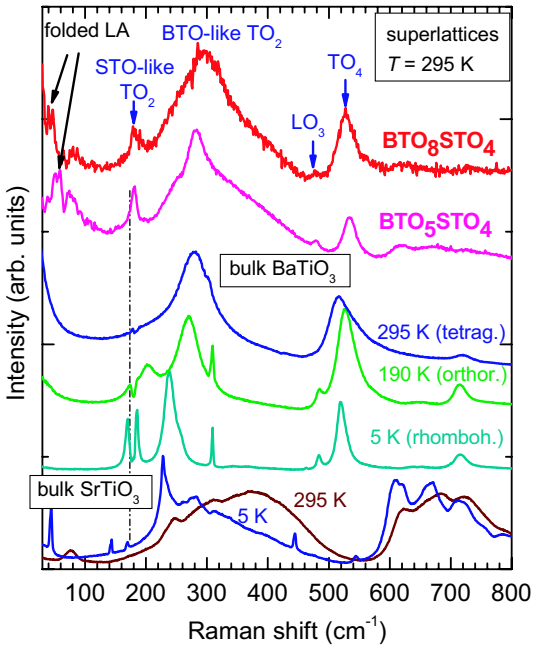

Figure S5. Raman spectra of the $(BTO_5/STO_4)\times25$ and $(BTO_8/STO_4)\times10$ superlattices at 295 K, measured with 351.1 nm laser line. The spectra of $BaTiO_3$ single crystals at 295, 190, and 100 K, corresponding to tetragonal, orthorhombic, and rhombohedral phases, respectively, and the spectra of $SrTiO_3$ single crystals at 295 and 5 K are shown for comparison. The bulk spectra were measured with the 514.5 nm laser line.

of the orthorhombic and rhombohedral phases of $BaTiO_3$, but not pronounced in the tetragonal phase.

The frequencies of several phonon branches in $SrTiO_3$ and $BaTiO_3$ are close to each other, and the phonons are not expected to be strongly localized within the thin $SrTiO_3$ and $BaTiO_3$ layers. According to first-principle calculations, these vibrations extend through the whole superlattice. This is the case for the LO_3 and the TO_4 modes, observed at about 478 and 530 cm^{-1}, respectively.

The line at about 180 cm^{-1} is attributed to the $SrTiO_3$-like TO_2 phonons. Its position corresponds closely to the TO_2 line in the electric-field-induced Raman spectrum of $SrTiO_3$ crystals *(7)* and in the 5 K spectrum of the $SrTiO_3$ single crystal. The first-order Raman lines are visible in these cases because the electric field and defects break the inversion symmetry in the $SrTiO_3$ crystals. The 180 cm^{-1} line is not from the $SrTiO_3$ substrate because the first-order Raman lines are symmetry-forbidden in bulk $SrTiO_3$ *(8)*. In fact, even the much stronger second-order features of the substrate at 230 and 610 cm^{-1} are barely seen in the UV Raman spectra. Although $BaTiO_3$ also has a feature due to the TO_1 mode of A_1 symmetry at about the same position (177 cm^{-1}), at room temperature (in the tetragonal phase) that feature is about 15-20 times weaker compared to the TO_2 and TO_4 lines, and it has a characteristic interference dip due to the coupling of the TO_1 and TO_2 modes of A_1 symmetry *(9)*. The 180 cm^{-1} line observed in the spectra of the superlattices is of the same order of magnitude in intensity as the TO_2 and TO_4 lines of $BaTiO_3$ and does not have the dip characteristic of $BaTiO_3$. Therefore, although we cannot absolutely rule out the contribution of the $BaTiO_3$ layers, we believe this line should be attributed to the phonons of the $SrTiO_3$ layers in the superlattices. The observation of the first-order Raman scattering by $SrTiO_3$ phonons indicates that the inversion symmetry is broken, and the $SrTiO_3$ layers in the superlattices are polar.

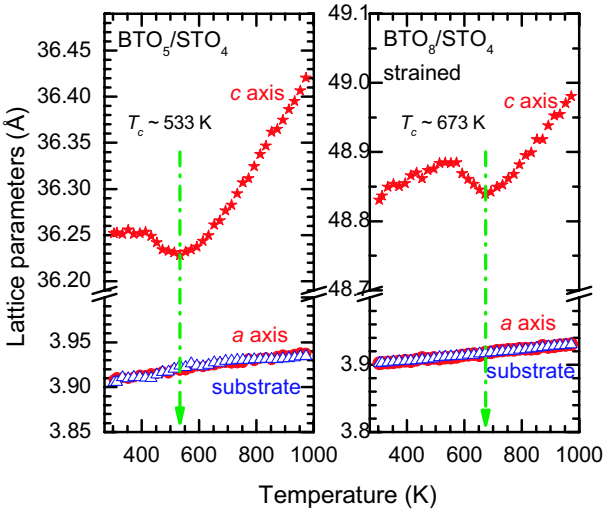

Figure S6. Temperature dependence of the lattice constants of the $(BTO_5/STO_4)\times25$ and $(BTO_8/STO_4)\times10$ superlattices and of the $SrTiO_3$ substrate, measured by x-ray diffraction..

4. Temperature-Dependent XRD Measurement

Two superlattice samples were measured by temperature-dependent XRD and the results are shown in Fig. S6. The a-axis lattice parameter of the superlattices overlap with that of the substrate, indicating that the superlattices are commensurately constrained to the $SrTiO_3$ substrate. The temperature dependence of the out-of-plane c-axis lattice parameter undergoes a change at $T =$ 533 and 673 K, which can be taken as an indication of T_c (*10–13*). The T_c values from the XRD measurement provides an additional confirmation of the Raman results.

References

S1. D. G. Schlom, *et al.*, *Mater. Sci. Eng. B* 87, 282 (2001).

S2. A. Soukiassian, *et al.*, *unpublished*.

S3. J. B. Nelson, D. P. Riley, *Proc. Phys. Soc. London* 57, 160 (1945).

S4. J. Menéndez, M. Cardona, *Phys. Rev. B* 29, 2051.

S5. G. Lang, *et al.*, *Phys. Rev. B* 59, 6182 (1999).

S6. D. A. Tenne, *et al.*, *Phys. Rev. B* 69, 174101 (2004).

S7. P. A. Fleury, J. M. Worlock, *Phys. Rev.* 174, 613 (1968).

S8. W. G. Nilsen, J. G. Skinner, *J. Chem. Phys.* 48, 2240 (1968).

S9. A. Scalabrin, A. S. Chaves, D. S. Shim, S. P. S. Porto, *Phys. Status Solidi B* 79, 731 (1977).

S10. E. D. Specht, H.-M. Christen, D. P. Norton, L. A. Boatner, *Phys. Rev. Lett.* 80, 4317 (1998).

S11. S. K. Streiffer, *et al.*, *Phys. Rev. Lett.* 89, 067601 (2002).

S12. M. Sepliarsky, S. R. Phillpot, M. G. Stachiotti, R. L. Migoni, *J. Appl. Phys.* 91, 3165 (2002).

S13. K. J. Choi, *et al.*, *Science* 306 (2004), 1005 (2004).